

Current Partition at Topological Channel Intersections

Zhenhua Qiao,^{1,2,3} Jeil Jung,^{3,4} Chungwei Lin,³ Yafei Ren,^{1,2} Allan H. MacDonald,³ and Qian Niu^{3,5}

¹*ICQD, Hefei National Laboratory for Physical Sciences at Microscale, University of Science and Technology of China, Hefei, Anhui 230026, China*

²*Department of Physics and Synergetic Innovation Center of Quantum Information and Quantum Physics, University of Science and Technology of China, Hefei, Anhui 230026, China*

³*Department of Physics, The University of Texas at Austin, Austin, Texas 78712, USA*

⁴*Graphene Research Centre and Department of Physics, National University of Singapore, 2 Science Drive 3, Singapore 117551, Singapore*

⁵*International Center for Quantum Materials and Collaborative Innovation Center of Quantum Matter, Peking University, Beijing 100871, China*

(Received 2 March 2013; revised manuscript received 15 February 2014; published 20 May 2014)

An intersection between one-dimensional chiral channels functions as a topological current splitter. We find that the splitting of a chiral zero-line mode obeys very simple yet highly counterintuitive partition laws that relate current paths to the geometry of the intersection. Our results have far reaching implications for electron beam splitter and interferometer device proposals based on chiral transport, and for understanding transport in systems in which multiple topological domains lead to a statistical network of chiral channels.

DOI: 10.1103/PhysRevLett.112.206601

PACS numbers: 72.80.Vp, 71.10.Pm, 73.43.Cd

The existence of topological channels has been proposed in a wide variety of systems including graphene mono- and bilayers [1–7], topological insulators with lattice dislocations [8], boron nitride crystals with grain boundaries [9], superfluid ³He [10], and photonic crystals [11,12]. The topological zero-line modes (ZLMs) that result from the reversal of mass signs in a chiral two-dimensional gas with quantized valley-Hall conductivity [2,3,10] can be viewed as realizations of Dirac zero energy modes [13,14] in a two-dimensional material. The valley Hall effect leads to conducting edge states and also, when the mass parameter varies spatially, to interior conducting states localized along mass zero lines [1–3,7]. Provided that intervalley scattering is weak the properties of these zero-line states are closely analogous [1–3] to those of quantum spin-Hall insulator edge states, and include in particular both chiral propagation and suppressed backscattering [1]. In this Letter, we examine the current partition properties at zero-line intersections [1,3], whether unintended in systems in which the mass term results from a disorder potential or from spontaneous symmetry breaking, or intended in devices based on ZLM properties.

The zero-line chiral channel [1–5] pattern with a spatially varying mass is schematically illustrated in Fig. 1(a). A mass term leading to the valley Hall effect [15,16] can be produced by a sublattice staggered external potential in monolayer graphene [4,5] and, more practically, by a gate-controlled interlayer potential difference in Bernal bilayer and ABC stacked multilayer graphene [1–3,6]. Mass terms can also be generated by spin-orbit coupling [17–19] and by electron-electron interaction [20–24]. In the last case ZLMs appear naturally at domain walls separating regions with different local anomalous, spin, or valley Hall conductivities [25].

Chiral propagation implies that ZLMs can propagate only in the direction which places negative masses either on their left *or* right side, depending on valley. It follows, as illustrated in Fig. 1(c), that there is no forward propagation at a zero-line intersection; a propagating mode is split between a portion that turns clockwise and a portion that turns counterclockwise. These unusual transport properties are potentially valuable for new types of electronic devices. We have carried out quantum transport calculations for an explicit model of intersecting ZLMs in order to discover the rules for current partitioning at ZLM splitter. The system we study is a π -band tight-binding model for monolayer graphene with a position-dependent sublattice-staggered potential constructed to form intersecting zero lines. The zero lines are connected with four reservoirs labeled as left (*L*), right (*R*), up (*U*), and down (*D*) in Fig. 1(b). For simplicity, we consider the case where the *U* and *D* ZLMs propagate vertically, while we vary the angle α between *R* and *D* ZLMs, and the angle β between *L* and *U* ZLMs. Smooth disorder potentials will tend to produce ZLM intersections with $\alpha = \beta$, corresponding to zero lines that are straight at the intersection point. The solid (blue) and dashed (red) lines in Fig. 1(b) indicate the allowed chiral propagation paths.

The numerical results reported on below are for a π -orbital tight-binding Hamiltonian with nearest neighbor hopping and a sublattice-staggered potential: $H = -t \sum_{\langle ij \rangle} c_i^\dagger c_j + \sum_{i \in A} U_{Ai} c_i^\dagger c_i + \sum_{i \in B} U_{Bi} c_i^\dagger c_i$. Here, c_i^\dagger (c_i) is a creation (annihilation) operator for an electron at site *i*, and $t = 2.6$ eV is the nearest neighbor hopping amplitude [26]. For a sublattice staggered potential the *A* and *B* sublattice energies are opposite, i.e., $U_{Ai} = -U_{Bi} = \lambda U_0$, where U_0 measures the potential

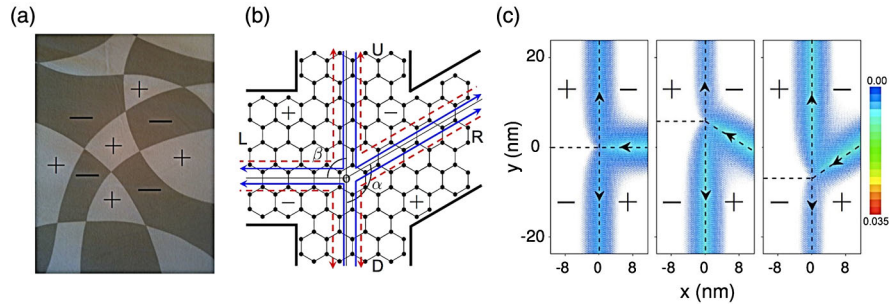


FIG. 1 (color online). Current partition at zero-line intersections: (a) Staggered sublattice-potential, and hence valley Hall conductivity, sign as a function of position. Sign changes define zero-line paths. (b) Schematic illustration of a four-terminal graphene sample containing zero lines. The “+” or “-” labels specify the sign of the staggered sublattice potential in each region. Left (L), right (R), up (U), and down (D) leads are connected to a rectangular central scattering region. The U and D zero lines are fixed along the vertical direction while the angles α and β specify the R and L zero-line directions. The thin solid lines in black denote zero lines. The blue solid and red dashed arrows represent allowed chiral propagation paths. (c) ZLM local density of states distribution for modes incident from lead R for $\alpha = 90^\circ, 60^\circ, 120^\circ$ at fixed $\beta = 90^\circ$.

strength and $\lambda = \pm$ is a mass parameter that specifies the sign of the valley Hall effect in each quadrant. In all our simulations, the potential amplitude was chosen to be $U_0/t = 0.05$. The ZLMs are confined to the lines cross which λ changes sign. The ZLM wave function tails spread into the bulk with a decay length proportional to the inverse of the mass U_0 [1,3].

Although our study has, for computational convenience, been carried out using a monolayer graphene model, we have confirmed that similar conclusions apply to ZLMs in bilayer graphene. The bilayer case is more interesting experimentally, because any desired mass pattern can be written with patterned external gates. Our transport calculations are based on the Landauer-Büttiker formalism [27] and recursively constructed Green’s functions [28,29]. The conductance from lead q to lead p is numerically evaluated from $G_{pq} = (e^2/h)\text{Tr}[\Gamma_p G^r \Gamma_q G^a]$, where e is the electron charge, h is the Planck’s constant, $G^{r,a}$ are the retarded and advanced Green’s functions [27], and Γ_p is a linewidth function describing the coupling between lead p and the central region. The propagation of ZLMs incoming from lead p is effectively illustrated by plotting a map of its contribution to the local density of states at an energy ε in the gap: $\rho_p(\mathbf{r}, \varepsilon) = 1/2\pi[G^r \Gamma_p G^a]_{rr}$, where \mathbf{r} is the real space coordinate. It is noteworthy the conductance doubles if the spin degree of freedom is included.

The central scattering region in our calculations is rectangular with size $n_x = 94$ and $n_y = 432$ as explained more fully in the Supplemental Material [31]. The valley label of a state is of course not a good quantum number for ZLMs and valleys are most strongly mixed when their wave vector projections in the propagation direction are identical. For energies inside the gap this coincidence happens only for propagation in the armchair direction [1,2,4,9]. However, numerical calculations have shown a remarkable absence of intervalley scattering at sharp turns in the zero line or at ZLM intersections [1] except

in a narrow energy range very close to the intervalley avoided crossing gap centered on $\varepsilon/t = 0.00$. For the results shown below we have chosen $\varepsilon/t = 0.01$ to avoid this energy range; the chirality of the ZLMs is then very well defined.

In a four-terminal ZLM splitter device [see Fig. 1(b)], there are in total twelve distinct interterminal conductance values. The number of independent conductances is reduced to six in time-reversal symmetric systems since $G_{pq} = G_{qp}$. For chiral transport, forward scattering and back scattering are absent at a ZLM intersection, further reducing the number of independent parameters. Furthermore, current conservation implies that $G_{pr} + G_{qr} = G_0 = e^2/h$ for any incoming lead r , where p and q are the labels of the two neighboring leads. It follows that

$$G_{LU} = G_{RD} \text{ \& \ } G_{RU} = G_{LD}, \quad (1)$$

and that $G_{RU} + G_{RD} = e^2/h$, leaving only one independent parameter for the entire four-terminal system. In a ZLM splitter with zero backscattering and perfect chiral current filtering, transport is completely characterized by specifying how the incoming current at an intersection is partitioned between the clockwise and counterclockwise rotation outgoing directions. The partition law must be the same for all incoming channels. The above relations were numerically verified for a ZLM current splitter with $\alpha = \beta = 90^\circ$ in Ref. [1] and we have now numerically verified that they are true for arbitrary values of the lead angles α and β (See the Supplemental Material [31] for further details).

In the following we focus on the partitioning, characterized by conductances G_{UR} and G_{DR} , of a current incident along the R lead between U and D outgoing channels. We first derive an approximate expression which explains why the current often follows the path requiring a larger rotation

angle [See Fig. 1(c)], and why current partition is dependent to a good approximation only on the junction geometry. Our qualitative argument is based on the properties of ZLMs in systems with two or more nearby parallel zero lines [30,31] separating regions with opposite signs of masses. Coupling between ZLMs traveling in opposite directions in this case leads to gaps in the traveling wave spectrum and to exponential decay along the zero line at energies in the gap. Analytic results can be obtained by matching constant mass solutions of the two-dimensional Dirac equation across zero lines at which the mass changes sign. For constant positive mass between and constant negative mass outside two zero lines separated by a distance d and oriented along the \hat{y} axis, we obtain the following compact expression for the wave function decay rate κ_x near the Dirac point:

$$\kappa_y = \kappa_0 \exp(-\kappa_x d),$$

where $\kappa_y = \sqrt{\kappa_0^2 - \kappa_x^2}$, $\kappa_0 = E_{\text{gap}}/(2v)$, v is the Fermi velocity, and E_{gap} is the energy gap in the limit of $d \rightarrow 0$. These equations imply a rapid crossover between two different regimes as a function of d . For $\kappa_0 d \ll 1$, $\kappa_y \sim \kappa_0$, and $\kappa_x \sim (2\kappa_0 d)\kappa_0$. The wave function amplitude decays rapidly along the channel, but is laterally extended. For $\kappa_0 d \gg 1$, on the other hand, $\kappa_x \sim \kappa_0$ and $\kappa_y \sim \kappa_0 \exp(-\kappa_0 d)$. In this limit, the wave functions are strongly localized near the zero lines and have negligible decay along the channel. Similarly, three zero-line modes are strongly coupled when they are all separated by much less than κ_0^{-1} . In this case, a single mode survives, which propagates in the majority travel direction and has weight equally partitioned between the two majority travel zero lines approximately. When four zero-line modes are separated by much less than κ_0^{-1} , the most slowly decaying modes weigh incoming and outgoing channels equally approximately.

We can apply these results to a ZLM approaching a junction along a zero line. The attenuation rate of the probability density implies a rate of scattering to an outgoing wave exiting the junction region along another zero line. As illustrated in Fig. 2, at a distance r from the junction, the separation between an adjacent pair of ZLMs is $d_{AB} = 2r \sin(\theta_{AB}/2)$, where θ_{AB} ($A, B = U, R, D, L$) is the angle between the A and B zero lines. At a given r , the local electronic structure can be approximated by accounting for the lateral separation between incoming and outgoing paths [See Fig. 2(b)]. In Fig. 2(c), we illustrate the evolution of the band structure near valley K for r varying from 40 to 10 nm at $\alpha = 150^\circ$. In the limit of small r , a gap starts to open. For $r < 10$ nm there are no propagating modes at energies close to the Dirac energy as anticipated from the discussion above.

Consider now the case of a ZLM incident from the right. We assume without loss of generality that $\alpha > 90^\circ$, i.e., that

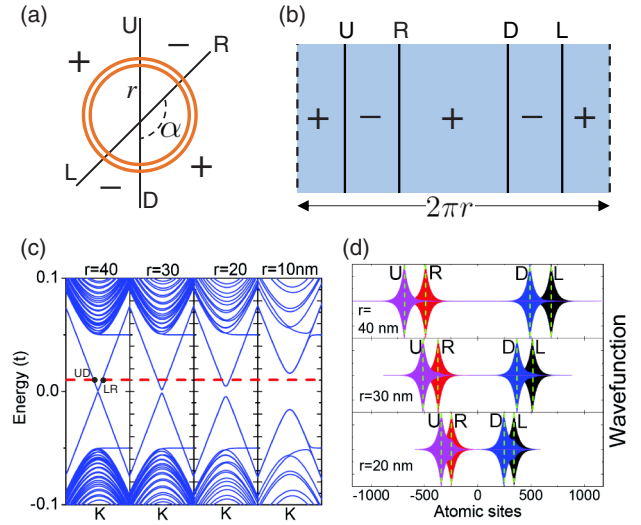


FIG. 2 (color online). Origin of the sharp-turn-favored partition rule: (a) Schematic representation of a straight zero-line intersection. The lateral separations between paths supporting ZLMs propagating in opposite directions decrease linearly as distance r from the junction decreases. For $\alpha \rightarrow 0$ and $\alpha \rightarrow 180^\circ$, the incoming ZLM is strongly coupled to the adjacent outgoing ZLM over a large range of r and is likely to be reflected by the junction. (b) At a given r channels A and B are separated by $2r \sin(\theta_{AB}/2)$ where θ_{AB} is the angle between A and B zero lines. The local electronic structure at each separation r can be approximated by one with colinear ZLMs. (c) Band structure near valley K for the one-dimensional mass variation illustrated in panel (b) for the cases of $\alpha = 150^\circ$ and $r = 40, 30, 20, 10$ nm. The red dashed line indicates the energy level $E = 0.01t$ for which we have performed our transport calculations. For $r \lesssim 10$ nm there are no propagating modes at this energy and electrons incoming along R must be scattered to U . (d) Wave functions along the four zero lines for radii $r = 40, 30, 20$ nm.

$\theta_{UR} < \theta_{DR}$. Then for $\beta > 180^\circ - \alpha$, $\theta_{UR} < \theta_{LU}$. It follows that with decreasing r , the incoming R channel is strongly coupled to the outgoing U channel, before the U channel is strongly coupled to the L channel. This asymmetric coupling situation persists for $\sin^{-1}(\theta_{LU}/2) < 2\kappa_0 r < \sin^{-1}(\theta_{UR}/2)$. Along this part of the path, electrons entering along the R channel are scattered to the U channel. For $2\kappa_0 r < \sin^{-1}(\theta_{LU}/2)$, all three channels are strongly coupled and the incoming mode begins to propagate without reflection, carried symmetrically between R and L channels. Asymmetric reflection occurs only along the outer segment. It follows that

$$G_{UR} \sim \frac{G_0}{2}(2 - P_T), \quad \text{and} \quad G_{DR} \sim \frac{G_0}{2}P_T, \quad (2)$$

where the probability of transmission through the asymmetric coupling region is approximated through

$$P_T \sim \exp[-2\kappa_0(r_0^> - r_0^<)] \\ = \exp[\sin(\theta_{LU}/2)^{-1} - \sin(\theta_{UR}/2)^{-1}], \quad (3)$$

with $r_0^< = [2\kappa_0 \sin(\theta_{LU}/2)]^{-1}$ and $r_0^> = [2\kappa_0 \sin(\theta_{UR}/2)]^{-1}$, where the prefactor $1/2$ in Eq. (2) leads to equipartition when $P_T = 1$ for $r_0^> = r_0^<$, consistently with the relation $G_0 = G_{UR} + G_{DR}$. Note that for $\theta_{UR} \rightarrow 0$, this probability vanishes and the incoming R ZLM is almost certainly scattered to the outgoing U ZLM.

For $\beta < 180^\circ - \alpha$, on the other hand, the U channel is already strongly coupled to the L channel when it is coupled to an incoming R ZLM. In this case scattering to the U outgoing channel can occur only when its coupling to the L channel is weak. It follows that

$$G_{UR} \sim \frac{G_0}{2} P_T, \quad \text{and} \quad G_{DR} \sim \frac{G_0}{2} (2 - P_T). \quad (4)$$

Note that these approximate conductances depend only on geometry, and are in good agreement with the numerical results summarized in Fig. 3(a). We emphasize that Eqs. (2) and (4) are approximate. They apply accurately only at energies close to the middle of the bulk energy gap. In our simulations, we have assumed that the potentials change abruptly at zero lines. When the potential changes smoothly the partition law changes slightly, but the counterintuitive characteristic, i.e., current paths tend to favor sharp turns, still holds [32].

Our results show a remarkable robustness to disorder which we modeled through site potential fluctuations given by $H_{\text{dis}} = \sum_i \omega_i c_i^\dagger c_i$ with ω_i uniformly distributed in the interval of $[-W/2, +W/2]$, where W characterizes the

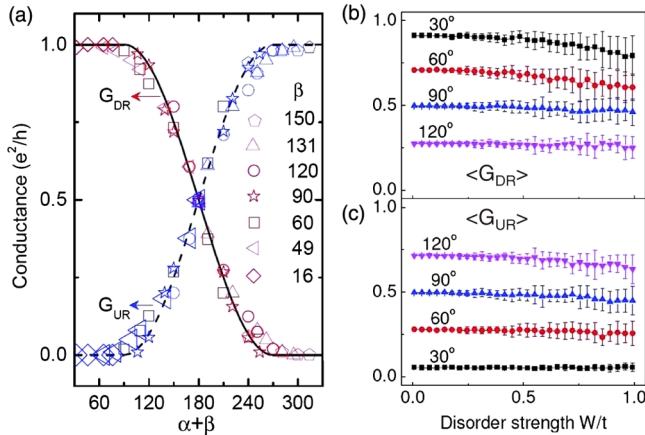


FIG. 3 (color online). Current partition law and effects of disorder. (a) Currents from the R zero line to the U and D zero lines as a function of $\alpha + \beta$ for the ZLM intersection defined in Fig. 1(c) at a series of β values. The current partition follows simple relations given in Eqs. (2) and (4) approximately. (b)–(c) Averaged conductances $\langle G_{DR} \rangle$ and $\langle G_{UR} \rangle$ calculated for $\beta = 90^\circ$ showing a remarkable robustness to disorder.

disorder strength. Our simulations shown in Figs. 3(b) and 3(c) suggest a remarkable robustness of our conclusions up to disorder strengths that are substantially larger than the bulk band gap $\Delta/t = 0.1$, suggesting promising prospects in experiments.

Since there are presently no practical techniques for imposing staggered sublattice potentials in single layer graphene, other closely related systems may ultimately be of greater experimental interest. In Bernal stacked bilayer graphene, for example, a ZLM splitter can be realized by using gates to achieve perpendicular electric fields which vary in sign spatially. Another possibility is 2D honeycomb photonic crystals, in which the Dirac points have been experimentally observed and sublattice staggered potentials can be realized by choosing different diameters for the cylinders which form the structure or by varying the dielectric material used.

In summary, when intervalley scattering can be neglected, transport along the zero lines of a sublattice-staggered potential in graphene is chiral, requiring travel in a direction which keeps positive masses on either the left or the right, depending on valley. We have used the Landauer-Büttiker formula and recursively constructed Green's functions to examine how chiral currents are partitioned between available outgoing leads at a ZLM intersection. We find that at energies near the middle of the bulk gap our numerical results for the dependence of the current partition on ZLM geometry are approximately described by a simple partition law specified in Eq. (2), and that the influence of disorder on this law is weak. The helicity of ZLM provides a new mechanism for allowing or blocking currents and may find applications in alternative designs for nanoelectronic devices or in enabling electron quantum interferometry [33] in a new setting. We have explored, for the first time to our knowledge, the geometry-dependent current partition laws at the intersection of two zero lines. It will be interesting to extend our present studies to more general parameter spaces and to look for similarities and differences with respect to other systems with chiral one-dimensional transport channels including photonic crystals, quantum anomalous Hall and quantum Hall effect systems, and chiral superconductors.

We are grateful to Wang-Kong Tse, Wang Yao, Jian Li, and Yue Yu for useful discussions and Peter J. Coulchinsky for his help with the figures. This work is financially supported by the Welch Foundation (F-1255 and TBF1473), and by DOE (Grant No. DE-FG03-02ER45958, Division of Materials Science and Engineering). Z. Q. and Y. R. are also financially supported by USTC Startup, Bairen Program of Chinese Academy of Sciences and NNSFC (Grant No. 91021019). J. J. also thanks for the support from the National Research Foundation of Singapore (NRF-NRFF2012-01). Q. N. acknowledges support from NBRPC (Grants No. 2012CB921300 and No. 2013CB921900), and

NSFC (Grant No. 91121004) during his leave at Peking University. The Computer Center of the University of Hong Kong is gratefully acknowledged for high-performance computing assistance.

-
- [1] Z. H. Qiao, J. Jung, Q. Niu, and A. H. MacDonald, *Nano Lett.* **11**, 3453 (2011).
- [2] J. Jung, F. Zhang, Z. H. Qiao, and A. H. MacDonald, *Phys. Rev. B* **84**, 075418 (2011).
- [3] I. Martin, Ya. M. Blanter, and A. F. Morpurgo, *Phys. Rev. Lett.* **100**, 036804 (2008).
- [4] G. W. Semenoff, V. Semenoff, and F. Zhou, *Phys. Rev. Lett.* **101**, 087204 (2008).
- [5] W. Yao, S. A. Yang, and Q. Niu, *Phys. Rev. Lett.* **102**, 096801 (2009).
- [6] M. Killi, S. Wu, and A. Paramekanti, *Phys. Rev. Lett.* **107**, 086801 (2011).
- [7] M. Zarenia, O. Leenaerts, B. Partoens, and F. M. Peeters, *Phys. Rev. B* **86**, 085451 (2012).
- [8] Y. Ran, Y. Zhang, and A. Vishwanath, *Nat. Phys.* **5**, 298 (2009).
- [9] J. Jung, Z. H. Qiao, Q. Niu, and A. H. MacDonald, *Nano Lett.* **12**, 2936 (2012).
- [10] G. E. Volovik, *The Universe in a Helium Droplet* (Oxford University Press, Oxford, 2003).
- [11] T. Ochiai and M. Onoda, *Phys. Rev. B* **80**, 155103 (2009).
- [12] A. B. Khanikaev, S. H. Mousavi, W.-K. Tse, M. Kargarian, A. H. MacDonald, and G. Shvets, *Nat. Mater.* **12**, 233 (2012).
- [13] R. Jackiw and C. Rebbi, *Phys. Rev. D* **13**, 3398 (1976).
- [14] W. P. Su, J. R. Schrieffer, and A. J. Heeger, *Phys. Rev. Lett.* **42**, 1698 (1979).
- [15] D. Xiao, W. Yao, and Q. Niu, *Phys. Rev. Lett.* **99**, 236809 (2007).
- [16] J. Li, I. Martin, M. Büttiker, and A. F. Morpurgo, *Nat. Phys.* **7**, 38 (2010).
- [17] Z. H. Qiao, S. A. Yang, W. Feng, W.-K. Tse, J. Ding, Y. Yao, J. Wang, and Q. Niu, *Phys. Rev. B* **82**, 161414 (2010).
- [18] C. L. Kane and E. J. Mele, *Phys. Rev. Lett.* **95**, 226801 (2005).
- [19] Z. H. Qiao, W.-K. Tse, H. Jiang, Y. Yao, and Q. Niu, *Phys. Rev. Lett.* **107**, 256801 (2011).
- [20] J. Jung, F. Zhang, and A. H. MacDonald, *Phys. Rev. B* **83**, 115408 (2011).
- [21] F. Zhang, J. Jung, G. A. Fiete, Q. Niu, and A. H. MacDonald, *Phys. Rev. Lett.* **106**, 156801 (2011).
- [22] J. Jung and A. H. MacDonald, *Phys. Rev. B* **84**, 085446 (2011).
- [23] R. Nandkishore and L. Levitov, *Phys. Rev. B* **82**, 115124 (2010).
- [24] V. Gurarie and A. M. Essin, *JETP Lett.* **97**, 233 (2013).
- [25] F. Zhang, J. Jung, and A. H. MacDonald, *J. Phys.: Conf. Ser.* **334**, 012002 (2011).
- [26] J. Jung and A. H. MacDonald, *Phys. Rev. B* **87**, 195450 (2013).
- [27] S. Datta, *Electronic Transport in Mesoscopic Systems* (Cambridge University Press, Cambridge, England, 1995).
- [28] M. P. Lopez Sancho, J. M. Lopez Sancho, and J. Rubio, *J. Phys. F* **14**, 1205 (1984).
- [29] J. Wang and H. Guo, *Phys. Rev. B* **79**, 045119 (2009).
- [30] T. Tudorovskiy and M. I. Katsnelson, *Phys. Rev. B* **86**, 045419 (2012).
- [31] See Supplemental Material at <http://link.aps.org/supplemental/10.1103/PhysRevLett.112.206601> for details. In the last section, we show another method to calculate the eigen energy of ZLMs which is different from Ref. [30] but more straightforward for step-kink potential as shown in our model.
- [32] Z. H. Qiao *et al.* (to be published).
- [33] Y. Ji, Y. Chung, D. Sprinzak, M. Heiblum, D. Mahalu, and H. Shtrikman, *Nature (London)* **422**, 415 (2003).